Dynamic Deformation of Pendant Drops on the Edge of High-Voltage Bushing Sheds Under Extreme Rainfall

LIN YANG [1], **(Member, IEEE), YIJIE SUN** [1], **YIFAN LIAO** [1,2], **ZHIQIANG KUANG** [1], **YANPENG HAO** [1], **(Member, IEEE), LICHENG LI** [1], **AND FUZENG ZHANG** [2]

[1] School of Electric Power, South China University of Technology, Guangzhou 510640, China
[2] Electric Power Research Institute, China Southern Power Grid, Guangzhou 510080, China

Corresponding author: Yanpeng Hao (yphao@scut.edu.cn)

ABSTRACT Flashover accidents on high-voltage bushings frequently occur under extreme rainfall, which is generally attributed to the bridging of adjacent sheds by pendant drops, a result of the dynamic deformation of pendant drops. We numerically investigate the effects of the parameters of pendant drops and the electric field on the dynamic deformation of pendant drops on a 500 kV transformer bushing under extreme rainfall and verify the simulation results by artificial rain experiment. The dynamic deformation of pendant drops is described by solving the Navier-Stokes equations and using the level set method. The results show that the maximum length of the pendant drop increases with the increase in the initial diameter and the initial mass flow rate, respectively, but decreases under the electric field. The main influencing factor on the maximum length of the pendant drop alters with the variation of the initial diameter and the initial mass flow rate in the absence of the electric field, whereas the initial mass flow rate is the unique main influencing factor in the presence of the electric field. Furthermore, the variations of the maximum length and breakup time of the pendant drop are elucidated by the instability of the pendant drop.

INDEX TERMS Flashover, high-voltage bushing, dynamic deformation, pendant drops, level set method, electric field, instability.

I. INTRODUCTION

A host of flashover accidents on high-voltage bushings and post insulators occur under rain, which threatens power system security severely [1]. Unfortunately, insulators may be confronted with more rain flashovers due to the frequent extreme rainfall weather affected by climate change [2].

Pendant drops on the edge of insulator sheds play a pivotal role in the whole process of rain flashovers [3], owing to partial discharge and decrease in flashover voltage caused by pendant drops [4]. The bridging of adjacent sheds by pendant drops is generally considered to be a main reason for rain flashovers [5]. It is noteworthy that the phenomenon that pendant drops bridge adjacent sheds is a result of the dynamic deformation of pendant drops.

Recently, the dynamic deformation of water droplets on the surface of composite insulator sheds has been studied extensively [6]–[10]. For example, Li *et al*. [6] performed experimental investigations of dynamic characteristics of water droplets on the surface of super-hydrophobic silicone rubber under a DC electric field, and Wei *et al*. [7] explored dynamic behaviors of water droplets on the super-hydrophobic surface under an AC electric field by numerical simulation and experiment. However, the dynamic deformation of pendant drops on the edge of insulator sheds has not been investigated, and it is significantly different from the dynamic deformation of water droplets on the surface of insulator sheds. Water droplets on the surface of insulator sheds move horizontally, subjected to an electric field force and surface tension,

---

The associate editor coordinating the review of this manuscript and approving it for publication was Jenny Mahoney.

whereas pendant drops on insulator sheds move vertically, which is affected by the gravity besides electric field force and surface tension [11]. Consequently, the dynamic deformation of pendant drops is more complicated.

Fortunately, the dynamic deformation of pendant drops on the edge of insulator sheds is similar to that of dripping drops and jets issuing from nozzles, as they move in the vertical direction likewise. The difference between dripping drops and jets lies in the flow rate, more precisely, dripping at a small flow rate and jetting at a large flow rate [12]. There are numerous researches on the dynamic deformation of dripping drops and jets in the field of fluid mechanics. For dripping drops, Subramani *et al.* [13] demonstrated that the lengths of dripping drops increase as the initial velocity of dripping drops increases in the absence of an electric field. The dynamic deformation of dripping drops under an electric field was studied by Nogueira *et al.* [14], Notz and Basaran [15], and Borthakur *et al.* [16], and these authors found that the lengths of dripping drops are affected by an electric field. For jets, Rajendran *et al.* [17] observed the dynamic deformation of jets without an electric field by high-speed camera and obtained the relationship among the maximum length of a jet, the nozzle diameter, the initial velocity, and the dimensionless number (Weber number). Son and Ohba [18] explored the instability of jets and found that the lengths of jets at breakup decrease with the increase in an electric field.

In the studies above, the dynamic deformation of dripping drops and jets is affected by various factors, such as the nozzle diameter, the initial velocity, and the electric field. For pendant drops on the edge of insulator sheds, the initial diameter of a pendant drop can be seen as an analogy of the nozzle diameter, and the initial velocity is replaced by the initial mass flow rate for the convenience in measurement. We explore how these factors affect the dynamic deformation of pendant drops on the edge of insulator sheds. Additionally, some differences between the present study and the studies above are necessary to be highlighted: (1) Dripping drops and jets move symmetrically, whereas pendant drops on insulator sheds move asymmetrically, as insulator sheds are tilted. (2) The electric field surrounding insulators is severely non-uniform, which is distinctly different from the electric field applied in the studies above.

To better understand the whole process of the bridging of adjacent sheds by pendant drops, we numerically investigate characteristics of the dynamic deformation of pendant drops on 500 kV bushing sheds under the effects of the initial diameter, the initial mass flow rate, and the electric field. The simulation results are also verified by artificial rain experiment. Subsequently, we explore the comprehensive effects of the initial diameter and the initial mass flow rate on the dynamic deformation of pendant drops in the absence and presence of an AC electric field. Finally, the reasons why these factors affect the dynamic deformation of pendant drops are discussed.
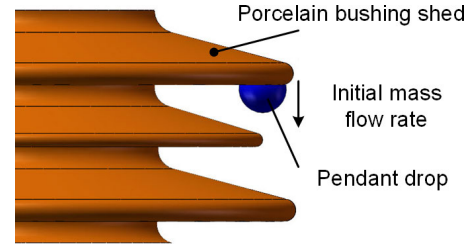

FIGURE 1. Simplified physical model. The initial shape of the pendant drop is a hemisphere, and the pendant drop initially moves at a constant mass flow rate.
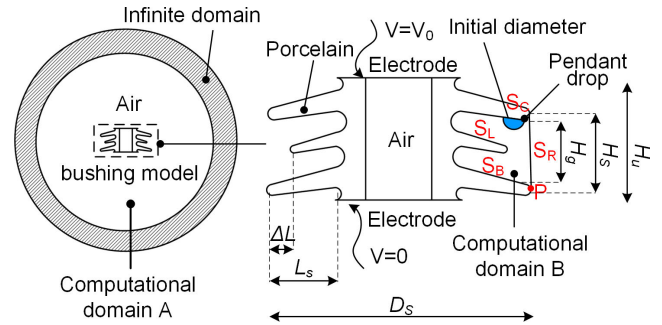

FIGURE 2. Simulation model.

II. SIMULATION
A. SIMULATION MODEL
In order to establish a simulation model, a simplified physical model based on a 500 kV hollow porcelain bushing was established first, as shown in Fig. 1. The process of rainwater gathering on the edge of insulator sheds is not considered for simplification. Hence, an idealized pendant drop is assumed to issue from the surface of the insulator shed at a constant mass flow rate, and its initial shape is a hemisphere whose diameter is considered as the initial diameter [16]. The main structural parameters of the 500 kV hollow porcelain bushing, as shown in Fig. 2, are listed in Table 1.

TABLE 1. Main structural parameters of a 500 kV hollow porcelain bushing.

H_s (mm)	H_g (mm)	H_u (mm)	D_S (mm)	L_s (mm)	ΔL (mm)
70	52	115	495	71	20

As shown in Fig. 2, H_s is the shed spacing distance; H_g is the actual air gap distance along the axis of the pendant drop between the adjacent sheds; H_u is the height of the unit of the 500 kV hollow porcelain bushing; D_S is the diameter of the large shed; L_s is the length of the large shed overhang; ΔL is the difference in length between the large shed overhang and the small one.

According to the simplified physical model and the main structural parameters of the high-voltage bushing in Table 1, a two-dimensional simulation model was established, as shown in Fig. 2. Good computational convergence and few modeling problems are the reasons for adopting the two-dimensional model. The whole simulation model is composed of two computational domains, A and B. The computational domain A includes a truncated air domain and a bushing model.

An infinite domain was set to ensure the accuracy of electric field calculations. The diameter of the computational domain A is $5D_S$ and the width of the infinite domain is D_S, where D_S is the diameter of the large bushing shed. To simplify the calculation, the bushing model consists of a unit of the 500 kV hollow porcelain bushing, a hemispherical pendant drop, and two thin electrodes on both sides of the unit of the porcelain bushing. The computational domain B consists of a hemispheric pendant drop and an air domain surrounded by a couple of adjacent sheds. The functions of these computational domains are as follows: (1) When effects of the initial diameter and the initial mass flow rate on the dynamic deformation of pendant drops without an electric field are investigated, the computational domain B is calculated. (2) When effects of the electric field on the dynamic deformation of pendant drops are studied, two computational domains, A and B, are simultaneously calculated.

B. SIMULATION METHOD

According to the simulation model, the dynamic deformation of a pendant drop on a 500 kV bushing shed is governed by the Navier-Stokes equations, and the interface of the pendant drop is tracked by level set method.

1) GOVERNING EQUATIONS OF THE DYNAMIC DEFORMATION OF A PENDANT DROP

Rainwater is an incompressible Newtonian fluid, and the flow of a pendant drop is assumed to be laminar. Hence, the dynamic deformation of a pendant drop is governed by the continuity equation and the Navier-Stokes equation [19], given as

$$\nabla \cdot \boldsymbol{u} = 0 \tag{1}$$

$$\rho \left(\frac{\partial \boldsymbol{u}}{\partial t} + \boldsymbol{u} \cdot \nabla \boldsymbol{u} \right) = -\nabla p + \mu (\nabla \boldsymbol{u} + (\nabla \boldsymbol{u})^{\mathbf{T}})$$
$$+ \boldsymbol{F}_g + \boldsymbol{F}_{st} + \boldsymbol{F}_E \tag{2}$$

where $\boldsymbol{u}$ is the velocity of fluids; ρ represents the density of fluids; t denotes time; p represents the pressure; μ is the hydrodynamic viscosity coefficient. $\boldsymbol{F}_g$ is the gravity given as $\boldsymbol{F}_g = \rho \, \boldsymbol{g}$, wherein $\boldsymbol{g}$ is the acceleration of the gravity. $\boldsymbol{F}_{st}$ is the body force based on the interfacial tension [20], given as

$$\boldsymbol{F}_{st} = \nabla \cdot [\delta(\boldsymbol{I} - \boldsymbol{n}\boldsymbol{n}^{\mathbf{T}})\gamma] \tag{3}$$

where γ is the surface tension coefficient; δ represents the Dirac delta function; $\boldsymbol{I}$ is the unit matrix; $\boldsymbol{n}$ represents the interface normal vector.

$\boldsymbol{F}_E$ is the electric body force based on the Maxwell tensor $\boldsymbol{T}_E$ [21], given as

$$\begin{cases} \boldsymbol{F}_E = \nabla \cdot \boldsymbol{T}_E \\ \boldsymbol{T}_E = \varepsilon \left[\boldsymbol{E} \otimes \boldsymbol{E} - \frac{1}{2} (\boldsymbol{E} \cdot \boldsymbol{E}) \boldsymbol{I} \right] \end{cases} \tag{4}$$

where ε is the permittivity and $\boldsymbol{E}$ is the electric field intensity.

In order to calculate $\boldsymbol{E}$, the governing equation for the electric field surrounding the high-voltage bushing in the presence of a pendant drop is presented. The charge conservation equation is [24]

$$\frac{\partial q}{\partial t} + \nabla \cdot \boldsymbol{J} = 0 \tag{5}$$

where $\boldsymbol{J}$ is the current density given as $\boldsymbol{J} = \sigma \, \boldsymbol{E}$, wherein σ is the conductivity; q is the bulk density of the induced charge of rainwater given as

$$\begin{cases} q = \nabla \cdot \boldsymbol{D} \\ \boldsymbol{D} = \varepsilon \boldsymbol{E} \end{cases} \tag{6}$$

Due to the low dynamic current generated in the electrostatic field, the magnetic effect is ignored, which can be expressed as

$$\begin{cases} \nabla \times \boldsymbol{E} = 0 \\ \boldsymbol{E} = -\nabla V \end{cases} \tag{7}$$

where V is the potential.

Finally, from (5) to (7), the governing equation for the quasi-static electric field is

$$\nabla \cdot \left(\varepsilon \frac{\partial \nabla V}{\partial t} + \sigma \nabla V \right) = 0 \tag{8}$$

2) LEVEL SET METHOD

Level set method is a numerical analysis for interface tracking and shape modeling [22]. The interface of a pendant drop is determined by the level-set function ϕ, expressed as $\phi = 0$ in the air and $\phi = 1$ in the pendant drop, and then it is represented as $\phi = 0.5$. The governing equation of the level set method is

$$\frac{\partial \phi}{\partial t} + \boldsymbol{u} \cdot \nabla \phi = \alpha \nabla \cdot \left(\beta \nabla \phi - \phi (1 - \phi) \frac{\nabla \phi}{|\nabla \phi|} \right) \tag{9}$$

where α is a re-initialization parameter given as $\alpha = u_{max}$, and β is an interface thickness control parameter given as $\beta = h_c/2$, wherein $u_{\max}$ is the maximum velocity of a pendant drop, and h_c is the size of a feature grid. Effects of β on the simulation results are discussed in Appendix.

As the level-set function ϕ is a smooth step function, the density of fluids ρ, the hydrodynamic viscosity coefficient μ, the permittivity ε, and the conductivity σ can be expressed by ϕ, given as

$$\begin{cases} \rho = \rho_a \phi + \rho_d (1 - \phi) \\ \mu = \mu_a \phi + \mu_d (1 - \phi) \\ \varepsilon = \varepsilon_a \phi + \varepsilon_d (1 - \phi) \\ \sigma = \sigma_a \phi + \sigma_d (1 - \phi) \end{cases} \tag{10}$$

where ρ_a and ρ_d are the density of air and drop, respectively; μ_a and μ_d are the viscosity of air and drop, respectively; ε_a and ε_d are the permittivity of air and drop, respectively; σ_a and σ_d are the conductivity of air and drop, respectively.

Significantly, a coupling of the flow field and the electric field is implemented based on the level set method. The flow field can be affected by the electric field. For example, the velocity of the pendant drop $\boldsymbol{u}$ varies with the electric

body force F_E in (2). For another, the flow field can alter the electric field as well. For instance, the level-set function ϕ varies with u in (9), and then the permittivity ε and the conductivity σ vary with ϕ likewise, which leads to the variation of the electric field.

C. SIMULATION SOLUTION

For solving the governing equations above, initial and boundary conditions were applied in the simulation model (Fig. 2). In the computational domain A, the electrodes were applied voltages, $V = V_0$ and $V = 0$, respectively. In the computational domain B, a line is added on the right side to form a finite domain. The boundary of the computational domain B is divided into S_C, S_L, S_R, and S_B. S_C is the contact line of the pendant drop and the bushing shed. S_L and S_R are the boundaries on the left and right side of S_C, respectively, and S_B is the bottom boundary. The slip-free condition and the no-penetration condition are applied at S_L, S_R, and S_B, given as

$$\begin{cases} u_n = 0 \\ u_t = 0 \end{cases} \quad (11)$$

where u_n and u_t are the normal and tangential velocity of the solid-liquid interface, respectively. S_C was set as the inlet of water flow, respectively. The boundary conditions, the constant flow rate, and the pressure point constraint condition ($p_0 = 0$) were applied at S_C and P, respectively. However, initial conditions of the three factors mentioned previously need to be obtained from an artificial rain experiment, and they are addressed in an upcoming section.

Comsol Multiphysics 5.4 was applied to simulate the dynamic deformation of a pendant drop on the 500 kV hollow porcelain bushing shed under extreme rainfall. The parameters of the materials in the simulation model are shown in Table 2. As this paper is engineering oriented and initial conditions are set as actual values in Comsol Multiphysics 5.4, all the equations are not non-dimensionalized.

TABLE 2. Material parameters.

Material	$\mathcal{E}_r$ (1)	σ (µS/cm)	ρ (kg/m³)	μ (Pa·s)
Porcelain	3.5	1.0×10^{-10}	—	—
Water	80.0	3.0×10^2	1.0×10^3	0.9×10^{-3}
Air	1.0	4.0×10^{-12}	1.0	1.8×10^{-5}

$\mathcal{E}_r$ is the relative permittivity; σ is the conductivity; ρ is the density of fluids; μ is the hydrodynamic viscosity coefficient.

The mesh generation of the simulation model is shown in Fig. 3. To reduce calculation and ensure the accuracy, the sizes of the maximum and minimum unit of the mesh in the computational domain A are 185 mm and 0.63 mm, respectively, and those in the computational domain B are 1.00 mm and 0.48 mm, respectively.

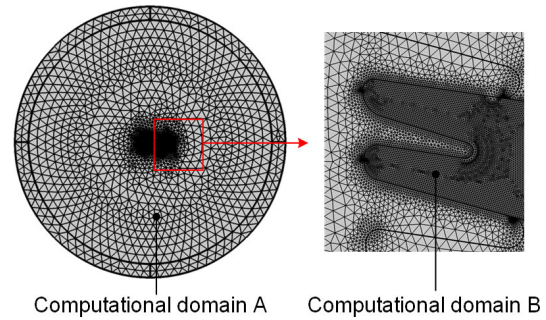The time integration scheme used in Comsol is presented in Appendix.

FIGURE 3. Mesh generation of the simulation model.
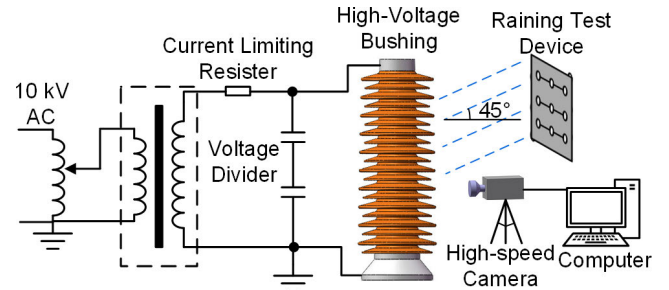

FIGURE 4. Schematic diagram of the artificial rain experiment.

III. EXPERIMENT

An artificial rain experiment on the 500 kV hollow porcelain bushing was carried out to provide the initial conditions of the three factors for simulation and verify the simulation results. The schematic diagram of the artificial rain experiment is shown in Fig. 4.

The voltages applied in the experiment were 0 kV and 318 kV, which represents that the 500 kV porcelain bushing works in the absence of voltage and the highest operating AC phase voltage, respectively. Due to extreme rainfall generally accompanied by strong winds, the artificial rainfall angle was set as 45° to simulate stormy weather. As rain flashover accidents typically occur within a few minutes of the onset of extreme rainfall, we are more concerned about instantaneous rainfall intensity, namely the total rainfall in one minute. By analyzing local one-minute rainfall data, the rainfall intensity in the experiment was set as 10 mm/min. The images of pendant drops were captured by high-speed camera (Vision Research Phantom v12.1, maximum resolution 1280 pixels $\times 800$ pixels). Moreover, we measured the critical length of a pendant drop before breaking up, defined as the maximum length of a pendant drop L_{max}, as shown in Fig. 5. The initial diameter of a pendant drop denoted as d_i is measured by image processing software. The initial mass flow rate represented as u_i is measured by mass flowmeter.

As the amount of rainwater is quite different in the upper, middle, and bottom bushing and affects u_i obviously, the high-voltage bushing was divided into Position A, B, and C. Moreover, due to the location of the raining test device, the high-voltage bushing was inevitably divided into two parts towards and back rain, respectively, as shown in Fig. 5. Consequently, the high-voltage bushing in the experiment was

TABLE 3. Statistics of initial diameters, initial mass flow rates, and maximum lengths of pendant drops.

Position		d_i (mm)		d_{ia} (mm)		u_i (g/s)		u_{ia} (g/s)		L_{maxa} (mm)		σ_L	
		0 kV	318 kV	0 kV	318 kV	0 kV	318 kV	0 kV	318 kV	0 kV	318 kV	0 kV	318 kV
A	A1	5.07~9.06	5.53~9.29	6.92	7.11	0.98~1.45	—	1.23	—	38.97	36.84	7.92	6.41
	A2	5.18~9.11	4.91~9.33	7.07	7.32	0.49~1.13	—	0.92	—	38.36	37.79	8.32	7.65
B	B1	4.87~9.14	5.83~9.19	6.96	7.12	1.33~2.03	—	1.71	—	42.87	39.96	5.29	7.13
	B2	4.92~9.08	5.94~9.15	7.08	7.15	1.30~2.01	—	1.63	—	44.49	40.01	6.12	6.59
C	C1	5.04~9.23	5.38~8.99	7.22	7.20	1.58~2.53	—	1.92	—	46.78	40.69	5.99	6.05
	C2	5.63~9.02	5.47~9.18	7.25	7.23	1.55~2.39	—	1.86	—	47.21	41.74	2.04	6.29

d_{ia} is the average of the initial diameters of pendant drops; u_{ia} is the average of the initial mass flow rate of pendant drops; L_{maxa} is the average of the maximum lengths of pendant drops; σ_L is the standard deviation of the maximum lengths of pendant drops. u_i and u_{ia} under 318 kV can not be measured due to the limit of the mass flowmeter.
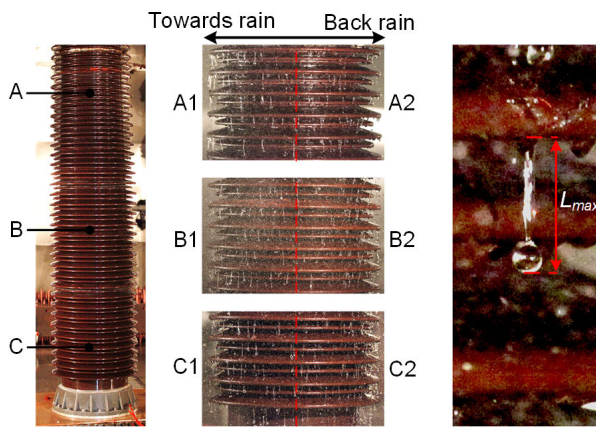
FIGURE 5. Images of pendant drops on the edge of bushing sheds in the artificial rain experiment.

FIGURE 6. Dynamic deformation of the pendant drop with the variation of the initial diameter. Two representative cases, $d_i = 5.00$ mm and 9.00 mm, are shown.

divided into six parts, A1, A2, B1, B2, C1, and C2 (Fig. 5). L_{max}, d_i, and u_i in A1, A2, B1, B2, C1, and C2 at the different applied voltages were measured, as listed in Table 3. The average of d_i, denoted as d_{ia}, and the average of u_i, represented as u_{ia}, were calculated to provide the initial conditions for simulation. Unfortunately, the initial mass flow rate of a pendant drop under 318 kV can not be measured due to the limit of the mass flowmeter. The average of L_{max}, denoted as L_{maxa}, was calculated to verify the simulation results in the following section. Besides, the standard deviation of L_{max} was calculated, given as
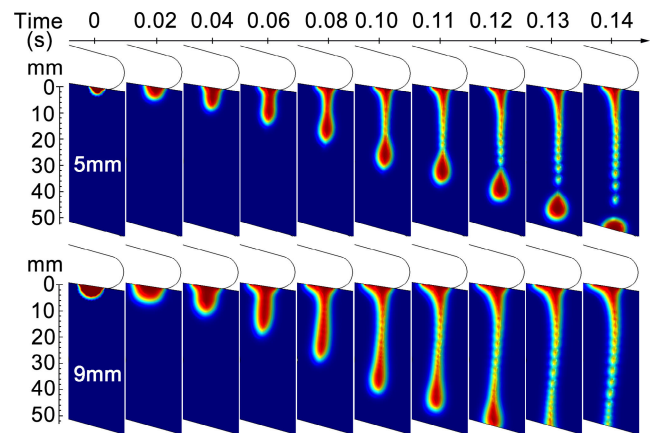
$$\sigma_L = \sqrt{\frac{1}{N}\sum_{i=1}^{N}(L_{maxi} - L_{maxa})} \qquad (12)$$

where N is the number of pendant drops measured, $N = 50$.

IV. SIMULATION RESULTS AND ANALYSIS
A. EFFECTS OF INITIAL DIAMETER ON DYNAMIC DEFORMATION OF PENDANT DROPS

In this section, the effects of the initial diameter d_i on the shape and lengths of pendant drops were investigated. To simulate the model in Fig. 2, the initial conditions of d_i, u_i, and V_0 need to be set, which can be obtained from the experiment. In Table 3, d_i ranges from 4.87 mm to 9.23 mm, and the average of u_{ia} in all positions is 1.55 g/s. For simplification, d_i was set as 5.00 to 9.00 mm at 1.00 mm interval, and u_i was

fixed at 1.55 g/s. Moreover, 0 kV was taken as the value of V_0 in the simulation model

To explore the dynamic deformation of the pendant drop with the variation of d_i, the time-dependent deformation of the pendant drop is depicted in Fig. 6, wherein two representative cases, $d_i = 5.00$ mm and 9.00 mm, are shown. In Fig. 6, the neck of the pendant drop prior to breakup becomes larger with the increase in d_i. For example, at $t = 0.10$ s, the average diameter of the neck of the pendant drop is 1.97 mm as $d_i = 5.00$ mm, whereas that is 2.38 mm as $d_i = 9.00$ mm. Additionally, the pendant drop breaks up before reaching the adjacent shed as $d_i = 5.00$ mm. By contrast, the pendant drop completely bridges the adjacent shed as $d_i = 9.00$ mm.

To quantitatively describe the dynamic deformation of the pendant drop, the time-dependent lengths of the pendant drop at the different d_i were computed, as shown in Fig. 7. The lengths of the pendant drop at different d_i all increase with time initially, then decrease, finally increase again. The maximum length of the pendant drop L_{max} increases with increasing d_i, which demonstrates that pendant drops bridge adjacent insulator sheds more easily as the initial diameter increases. Additionally, the pendant drop breaks up at $t = 0.11$ s, as $d_i < 9.00$ mm, while it breaks up at $t = 0.12$ s, as $d_i = 9.00$ mm, indicating that the breakup time of the pendant drop tends to increase with increasing d_i.

To verify the simulation results, we chose the simulation results of L_{max}, one of the parameters of the dynamic deformation of pendant drops, to compare with L_{maxa} derived from the experiment. As the initial mass flow rate in the experiment is uncontrollable and u_{ia} in B2 (Table 3) is close to 1.55 g/s, L_{maxa} in B2 (Table 3) was chosen to compare with L_{max} obtained from the simulation. Due to the random form of pendant drops on the edge of the bushing sheds, d_i in the experiment is uncontrollable. We chose L_{maxa} at d_i = 4.50-5.50 mm, 5.51-6.50 mm, 6.51-7.50 mm, 7.51-8.50 mm, and 8.51-9.50 mm in B2 to compare with L_{max} at d_i = 5.00 mm, 6.00 mm, 7.00 mm, 8.00 mm, and 9.00 mm in the simulation. The comparisons between the simulation results and the experimental results are presented in Fig. 8. The relative error is expressed as

$$e_r = \left| \frac{\Delta L_{max}}{L_{maxa}} \right| \tag{13}$$

where ΔL_{max} is the difference between L_{max} and L_{maxa}. The maximum relative error occurring as d_i = 9.00 mm is 12.9%, which indicates that the simulation results are relatively accurate.

To further reveal the quantitative relationship between L_{max} and d_i, the simulation results in Fig. 8 were fitted. The quantitative relationship is expressed as

$$L_{max} = 14.04 + 4d_i \tag{14}$$

Here, the correlation coefficient R^2 is 0.9446, which demonstrates that the quantitative relationship is reasonable.

B. EFFECTS OF INITIAL MASS FLOW RATE ON DYNAMIC DEFORMATION OF PENDANT DROPS

The variations of the shape and lengths of pendant drops with different u_i were explored in this section. The initial conditions of d_i, u_i, and V_0 are determined by the results of the experiment. In Table 3, u_i ranges from 0.49 g/s to 2.53 g/s, and the average of d_{ia} in all positions is 7.08 mm. Therefore, for simplification, u_i was set as 0.50 to 2.50 g/s at

FIGURE 8. Verification of the simulation results. The fitted curve shows the quantitative relationship between the maximum length of the pendant drop and the initial diameter.
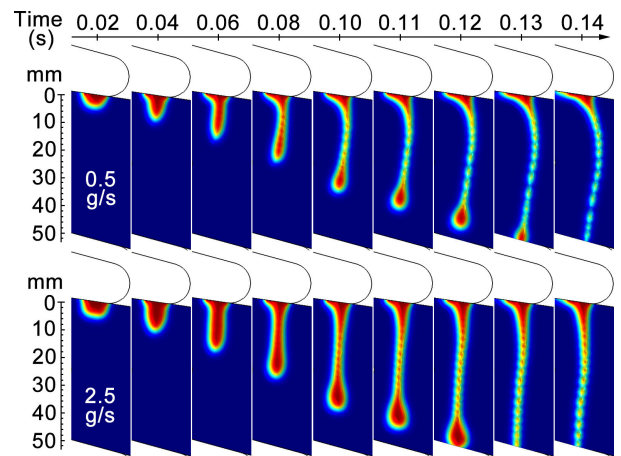
FIGURE 9. Dynamic deformation of the pendant drop with the variation of the initial mass flow rate. Two representative cases, u_i = 0.50 g/s and 2.50 g/s, are shown.

0.50 g/s interval, and d_i was fixed at 7.00 mm. Besides, V_0 was fixed at 0 kV.

The deformation of the pendant drop at the different u_i with time was studied, as shown in Fig. 9, wherein two representative cases, u_i = 0.50 g/s and 2.50 g/s, are shown. In Fig. 9, before the breakup of the pendant drop, the average diameter of the neck of the pendant drop increases with the increase in u_i. Furthermore, the pendant drop seems to be more unstable as u_i = 0.50 g/s. For example, the pendant drop breaks up at 0.10 s, as u_i = 0.50 g/s, whereas it does not break up until t = 0.12 s, as u_i = 2.50 g/s.

To quantitatively address the dynamic deformation of the pendant drop, the time-dependent lengths of the pendant drop at different u_i were computed, as shown in Fig. 10. The variations of the lengths of the pendant drop at the different u_i are similar to those at the different d_i. Moreover, L_{max} increases with the increase in u_i, which indicates that pendant drops are more likely to bridge adjacent insulator sheds as the initial mass flow rate increases. Additionally, the breakup time of the pendant drop increases with the increase in u_i.
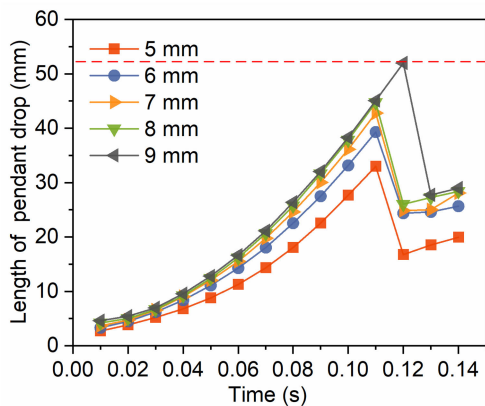
FIGURE 7. Lengths of the pendant drop at the different initial diameters varying with time. The red dashed line represents the bridging of the adjacent bushing shed by the pendant drop.
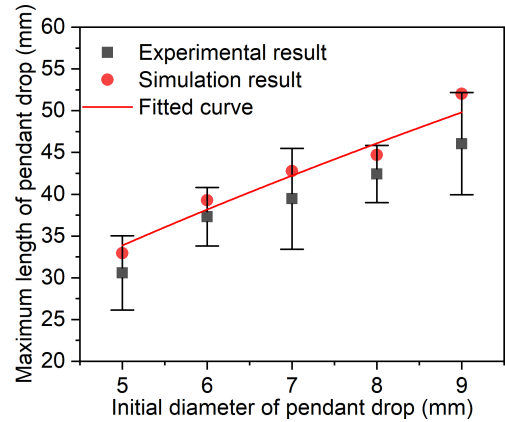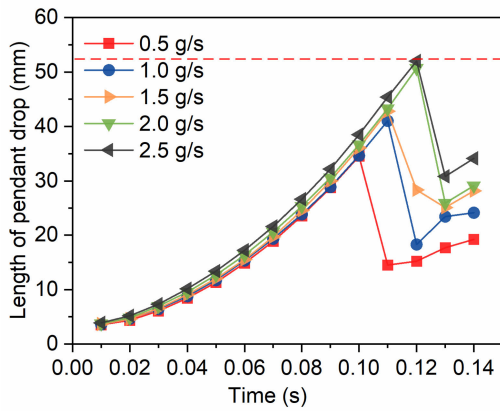
FIGURE 10. Lengths of the pendant drop at the different initial mass flow rates varying with time. The red dashed line represents the bridging of the adjacent bushing shed by the pendant drop.
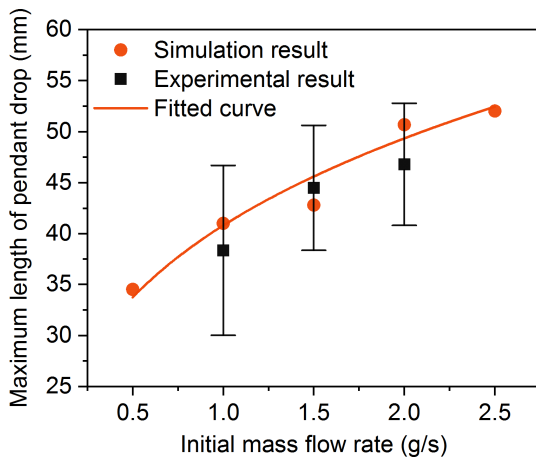

FIGURE 11. Verification of the simulation results. The fitted curve represents the quantitative relationship between the maximum length of the pendant drop and the initial mass flow rate.

For the verification of the simulation results, L_{max} was chosen as an object of comparison. However, L_{max} at a given u_i in the experiment can not be measured, as pendant drops on the edge of the bushing sheds form randomly. Accordingly, we first chose L_{maxa} in A2, B2, and C1 (Table 3) to verify a part of L_{max} derived from the simulation, as u_{ia} in A2, B2, and C1 (Table 3) are close to 1.00 g/s, 1.50 g/s, and 2.00 g/s, respectively. Subsequently, L_{maxa} at d_i = 6.50-7.50 mm in these parts, were compared with L_{max} at u_i = 1.00 g/s, 1.50 g/s, and 2.00 g/s in the simulation, respectively. The comparisons between the simulation results and the experimental results are shown in Fig. 11. The maximum error occurring as u_i = 2.00 g/s is 8.34%, which indicates that the simulation results are accurate.

To derive a quantitative relationship between L_{max} and u_i, the simulation results of L_{max} with the variation of u_i were fitted. The quantitative relationship is

$$L_{max} = 40.76u_i^{0.26} \qquad (15)$$

Here, the correlation coefficient R^2 is 0.9519, which demonstrates that the quantitative relationship above is reasonable.
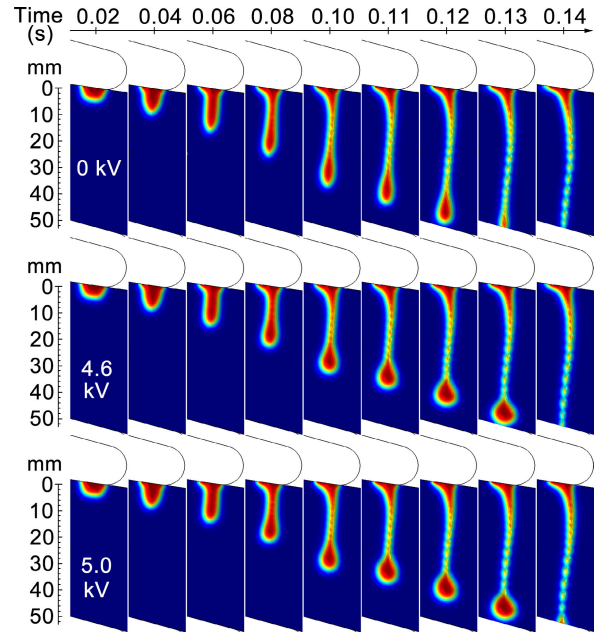

FIGURE 12. Dynamic deformation of the pendant drop with the variation of the applied voltage. Three representative cases, $V_0 = 0$ kV, 4.60 kV, and 5.00 kV, are shown.

C. EFFECTS OF ELECTRIC FIELD ON DYNAMIC DEFORMATION OF PENDANT DROPS

In this section, the shape and lengths of pendant drops, affected by an electric field, were investigated. The initial diameter d_i and the initial mass flow rate u_i were set as 7.00 mm and 1.55 g/s, respectively, which has been explained in the sections above. The operating AC phase voltage of the 500 kV bushing is 289 kV, and 318 kV (Table 3) is taken as the highest operating AC phase voltage. For simplification, the voltage distribution along the 500 kV hollow porcelain bushing is considered to be uniform. Hence, the voltage applied at the unit of the 500 kV hollow porcelain bushing (Fig. 2) was set as 4.60 kV to 5.00 kV at 0.20 kV interval.

Fig. 12 presents the time-dependent deformation of the pendant drop with the variation of the applied voltages, wherein three representative cases, $V_0 = 0$ kV, 4.60 kV, and 5.00 kV, are shown. The shape of the pendant drop before breakup becomes nearly spherical under 4.60 kV and 5.00 kV. The average diameter of the neck of the pendant drop barely changes with the increase in the applied voltage.

To quantitatively describe the dynamic deformation of the pendant drop, the lengths of the pendant drop under the different applied voltages with time were computed, as shown in Fig. 13.

Fig.13 shows that the lengths of the pendant drop initially increase, subsequently decrease, and finally increase with time under the different applied voltages, which is similar to the cases at the different d_i and u_i. Compared with L_{max} under 5.00 kV, L_{max} under 4.60 kV and 4.80 kV changes by only 4.8%, which indicates that L_{max} has little change under the fluctuation of the operating voltage. Moreover, compared with L_{max} under 0 kV, L_{max} under the other applied voltages
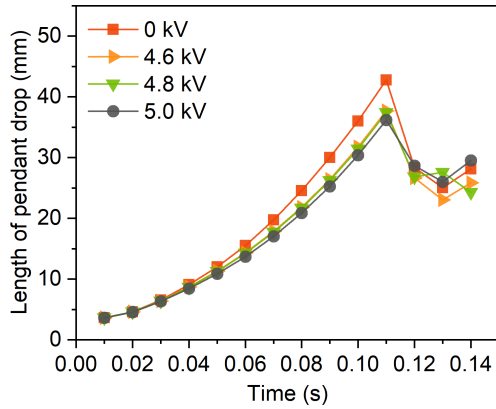
FIGURE 13. Lengths of the pendant drop under the different applied voltages varying with time.
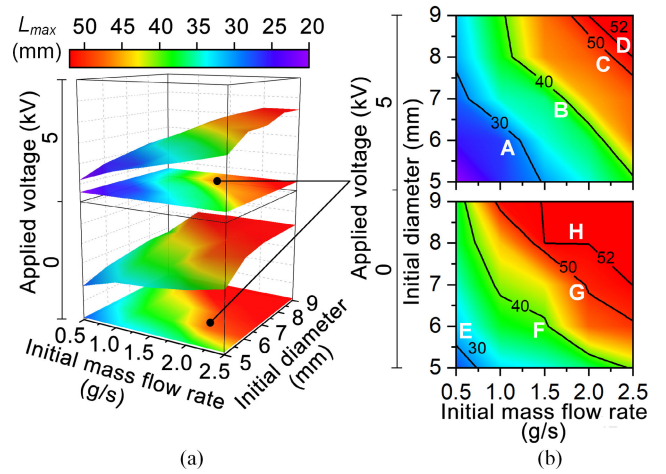

FIGURE 14. Variations of the maximum length of the pendant drop under the different initial diameters, initial mass flow rates, and applied voltages. a is a three-dimensional diagram that is divided into two parts by the applied voltages. b is a contour diagram of the maximum lengths of the pendant drop corresponding to a. A-H are the contours of the maximum lengths of the pendant drop. The maximum lengths of the pendant drop under 5 kV denoted by A, B, C, and D are the same as those under 0 kV represented by E, F, G, and H, respectively.

decrease, indicating that the electric field leads to a reduction in L_{max}. Additionally, the breakup time of the pendant drop seems to change rarely within the applied voltage range.

In order to verify the simulation results, L_{max} derived from the simulation were compared with L_{maxa} obtained from the experiment. However, L_{maxa} under the different applied voltages at the given mass flow rate, 1.55 g/s, can not be derived. Considering that u_{ia} in B2 is close to 1.55 g/s, and the fluctuation of the operating voltage has little effect on L_{max}, L_{max} under 5.00 kV was compared with L_{maxa} under 318 kV in B2 (Table 3). The relative error is 9.7%, demonstrating that the simulation results are accurate.

D. COMPREHENSIVE EFFECTS OF MULTIPLE FACTORS ON DYNAMIC DEFORMATION OF PENDANT DROPS

The previous sections explored the effects of the three factors on the dynamic deformation of pendant drops separately. To accords with the reality, the comprehensive effects of the initial diameter, the initial mass flow rate, and the electric field on L_{max} were studied in this section. In accordance with the previous sections, d_i and u_i were set as 5.00 to 9.00 mm at 1.00 mm interval, 0.50 to 2.50 g/s at 0.50 g/s interval, respectively. Considering the fluctuation of the operating voltage barely affects L_{max}, 0 kV and 5 kV were imposed in the simulation model, respectively.

Fig. 14 illustrates the variations of L_{max} under the three factors. The relationship between L_{max}, and d_i, u_i, and V_0 can be obtained from Fig. 14a, given as

$$L_{max} = \begin{cases} -3.7 + 10u_i + 3.8d_i & V_0 = 5kV \\ -35 + 18u_i + 14d_i - 3.2u_i^2 - 0.76d_i^2 & V_0 = 0kV \end{cases}$$
(16)

In Fig. 14a, L_{max} under 0 kV and 5 kV both increase as d_i and u_i simultaneously increase. In Fig. 14b, the variations of contours are different not only under the same applied voltage, such as A-E, but also under the different applied voltages, such as B and F, which indicates that d_i and u_i affect L_{max} in the presence and absence of the electric field with different degrees.

For the sake of exploring the main influencing factor of L_{max} between d_i and u_i, an absolute value of the ratios of the gradient of d_i and u_i in A-H (Fig. 14b) is taken as a criterion given as

$$k = \left| \frac{\Delta d_i}{\Delta u_i} \right|$$
(17)

where Δd_i and Δu_i are the gradient of d_i and u_i, respectively. For $k > 1$, u_i is the main influencing factor; for $k = 1$, d_i and u_i have the same effect; for $k < 1$, d_i is the main influencing factor. The main influencing factor of L_{max} under the different applied voltages was analyzed, as listed in Table 4.

In Table 4, without an electric field, the main influencing factor of L_{max} is different among the contours, E-H. For example, u_i plays a decisive role in affecting L_{max} by analyzing the variation of the contour E, whereas the initial diameter d_i contributes more to affecting L_{max} in some ranges of u_i and d_i in F-H. In contrast, the main influencing factor of L_{max} is unique under the electric field, which indicating that the electric field seems to alter the effect of u_i or d_i on L_{max}. Although some contours, such as B and F, represent the same L_{max} under the different applied voltages, there are several distinctions in their main influencing factors. For example, the main influencing factor of L_{max} in F varies with the range of u_i and d_i, whereas that in B is unique. Additionally, an exceptional value of k needs to be highlighted. As $u_i = 1.50$ to 2.00 g/s and $d_i = 8.00$ mm in H, the value of k is 0, which indicates that L_{max} does not alter with increasing u_i, as $d_i = 8.00$ mm.

V. DISCUSSION

In terms of the bridging of adjacent sheds by pendant drops, the maximum length of a pendant drop L_{max} is the most significant parameter of the dynamic deformation of pendant

TABLE 4. Main influencing factor of the maximum length of the pendant drop between the initial diameter and the initial mass flow rate in the presence and absence of the electric field.

Applied voltage (kV)	Contour	Initial mass flow rate (g/s)	Initial diameter (mm)	k	Main influencing factor
5	A	0.50-0.70	7.00-7.65	3.25	u_i
		0.70-1.25	6.00-7.00	1.82	u_i
		1.25-1.50	5.00-6.00	4.00	u_i
	B	1.05~1.18	8.00-9.00	7.70	u_i
		1.18-2.50	5.10-8.00	2.20	u_i
	C	1.80~2.50	7.55~9.00	2.07	u_i
	D	2.00~2.50	8.00~9.00	2.00	u_i
0	E	0.50-0.75	5.00~5.50	2.00	u_i
		0.63-0.70	8.00-9.00	14.29	u_i
		0.70-1.00	6.75-8.00	4.17	u_i
	F	1.00-1.50	6.35-6.75	0.80	d_i
		1.50-1.55	6.00-6.35	7.00	u_i
		1.55-2.00	5.40-6.00	1.33	u_i
		2.00-2.40	5.00-5.40	1.00	u_i and d_i
		0.95-1.95	7.00-9.00	2.00	u_i
	G	1.95-2.00	6.80-7.00	4.00	u_i
		2.00-2.50	6.30-6.80	1.00	u_i and d_i
		1.45-1.50	8.00-9.00	20.00	u_i
	H	1.50-2.00	8.00-8.00	0	d_i
		2.00-2.50	7.05-8.00	1.90	u_i

drops. In Section IV, L_{max} increases with the increase in the initial diameter and the initial mass flow rate but decreases as the electric field increases. These results can be elucidated by pressure and instability, according to the Rayleigh model.

A small disturbance on the surface of pendant drops always exists in the whole process of the dynamic deformation of pendant drops [25], which leads to the formation of a wave-like surface, as shown in Fig. 15a. As a result, there is an additional pressure P_S on the concave and convex surface, respectively [26], as shown in Fig. 15b. The additional pressure in the convex surface A and the concave surface B without an electric field, P_{SA} and P_{SB}, can be expressed as

$$P_{SA} = P_{dA} - P_{aA} \qquad (18)$$
$$P_{SB} = P_{aB} - P_{dB} \qquad (19)$$

where P_{dA} and P_{dB} are the internal pressure of the pendant drop at A and B, respectively, and P_{aA} and P_{aB} are the air pressure around the pendant drop at A and B, respectively.

According to the Young-Laplace formula, the additional pressure of arbitrary curved surface is [26]

$$P_S = \gamma(\frac{1}{R_1} + \frac{1}{R_2}) \qquad (20)$$

where R_1 and R_2 are the curvature radius of any pair of normal sections, as shown in Fig. 15c. R_1 at A and B are expressed as $R_{1A} = R_0 + A$ and $R_{1B} = R_0 - A$, respectively. R_2 at A and

B can be calculated by

$$R = \left| \frac{(1 + f_x'^2)^{3/2}}{f_x''} \right| \qquad (21)$$

where f_x is a curve function of the disturbed surface of the pendant drop given as [25]

$$f_x = d + A_m \sin(2\pi x/\lambda) \qquad (22)$$

wherein d is the diameter of the idealized neck of the pendant drop without any disturbance, as shown in Fig. 15a. A_m represents the maximum amplitude of the disturbance. λ denotes the wavelength of the disturbance

Based on (21) and (22), R_1 and R_2 at A and B are $R_{2A} = \lambda^2/(4\pi^2 A_m)$ and $R_{2B} = \lambda^2/(4\pi^2 A_m)$, respectively. Then P_{SA} and P_{SB} calculated by (20) are

$$P_{SA} = \gamma(\frac{1}{d + A_m} + \frac{4\pi^2 A_m}{\lambda^2}) \qquad (23)$$

$$P_{SB} = \gamma(\frac{1}{d - A_m} - \frac{4\pi^2 A_m}{\lambda^2}) \qquad (24)$$

Finally, the difference between the additional pressures ΔP is

$$\Delta P = P_{SA} - P_{SB}$$
$$= \gamma \left(\frac{8\pi^2 A_m}{\lambda^2} - \frac{2A_m}{d^2 - A_m^2} \right) \qquad (25)$$

ΔP reflects the instability of pendant drops. Specifically, pendant drops break up more easily with the decrease in ΔP. Equation (25) indicates that ΔP increases with increasing d. As a result, the instability of pendant drops is reduced, and then pendant drops are not easy to break up. In Section IV, before the breakup of the pendant drop, the neck of the pendant drop becomes larger with the increase in d_i and u_i. Namely, d in Fig. 15a increases with increasing d_i and u_i. Consequently, the maximum length of the pendant drop increases as the initial diameter and the initial mass flow rate increase.

Considering an electric field surrounding the pendant drop, one more pressure generated by an electric field appears on the concave and convex surface, as shown in Fig. 15b, and the additional pressure at A and B, P_{SA1} and P_{SB2} are

$$P_{SA1} = P_{dA} - P_{aA} - P_E \qquad (26)$$
$$P_{SB1} = P_{aA} + P_E - P_{dA} \qquad (27)$$

where P_E is the pressure generated by an electric field.

Thus, the difference between the additional pressures under an electric field ΔP_1 is

$$\Delta P_1 = P_{SA} - P_{SB}$$
$$= (P_{dA} + P_{dB}) - (P_{aA} + P_{aB}) - 2P_E \qquad (28)$$

ΔP_1 decreases in the presence of an electric field, according to (28). Hence, pendant drops become more unstable, and then pendant drops under an electric field break up more
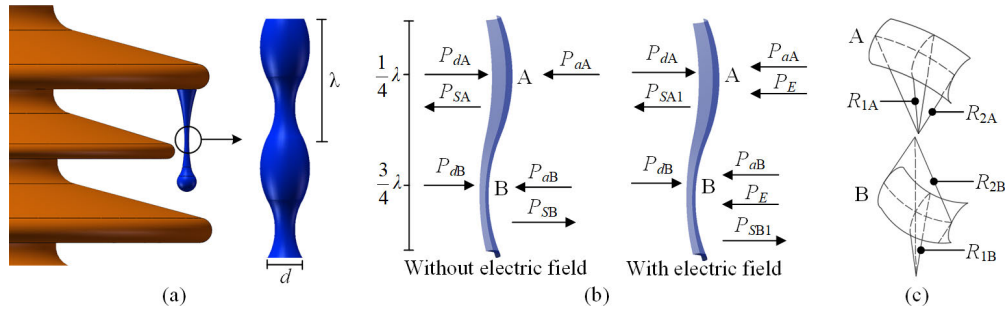
FIGURE 15. Schematic diagram of the pressure and instability of a pendant drop. (a) Disturbance of a pendant drop on a high-voltage bushing shed. (b) Additional pressure in the convex surface A and the concave surface B in the absence and presence of an electric field. (c) The curvature radius of a pair of normal sections at A and B.

easily than those without an electric field. Naturally, the maximum length of the pendant drop decreases with increasing the intensity of the electric field.

Additionally, the variations of the breakup time of the pendant drop under the three factors are different, which can also be explained by instability. The instability of the pendant drop decreases with increasing d_i and u_i, which delays the breakup time of the pendant drop. Similarly, the instability of the pendant drop increases as the electric field surrounding the pendant drop increases, indicating that the pendant drop breaks up in advance. However, this seems to be the contradiction with that in Fig. 13. The relationship between the surface tension of water droplets and the applied voltage studied by Baten *et al.* demonstrates that the surface tension does not increase significantly within the range of 4.00 kV to 5.00 kV [14]. Based on the breakup time of jets t_b [25], given as

$$ t_b \propto \sqrt{\frac{\rho d_i^3}{\gamma}} \qquad (29) $$

the breakup time of the pendant drop does not decrease obviously as surface tension increases barely.

Some paradoxical results obtained from the experiment and the simulation are necessary to be highlighted. We observed that the maximum value of L_{maxa} under 318 kV is 41.74 mm in Table 3, and in Fig. 14, L_{max} under 5.00 kV derived from the simulation is 52 mm, only as $u_i = 2.00$ to 2.50 g/s, and $d_i = 8.00$ to 9.00 mm. These results show that in most instances, the maximum lengths of pendant drops are rarely up to 52 mm, the actual air gap distance along the axis of the pendant drop between the adjacent sheds, indicating that pendant drops often break up before completely bridging adjacent sheds. However, this inference is not well consistent with the conclusion that rain flashover was mainly caused by the bridge of adjacent sheds by pendant drops in [5]. Moreover, the shed spacing distance of the tapered porcelain insulator in [5] is 90 mm, longer than that of porcelain bushing in our experiment, and the rainfall intensity is lower than that in our experiment, which suggests that pendant drops seemingly bridges adjacent sheds more easily in our study. A possible reason for this contradiction is that the observers may be misled by broken pendant drops. For

instance, in Fig. 12, the adjacent shed is seemingly bridged by the broken pendant drop under 4.60 kV as $t = 0.13$ s, rather than by a complete pendant drop. Thereby, we suppose that the phenomenon that a complete pendant drop bridges an adjacent shed under extreme rainfall occurs infrequently. On this basis, the dynamic deformation of pendant drops may provide a fresh idea for future study on the rain flashover mechanism.

VI. CONCLUSION
The dynamic deformation of pendant drops on 500 kV bushing sheds under extreme rainfall has been investigated by simulation. The study focuses on the effects of the initial diameter, the initial mass flow rate, and the electric field on the shapes and lengths of pendant drops. The main conclusions are as follows:

1) As the initial diameter and the initial mass flow rate increase, the neck of the pendant drop becomes larger, which reduces the instability of the pendant drop. Under the electric field, the shape of the pendant drop before breakup becomes nearly spherical, and there is little variation in the neck of the pendant drop.

2) The maximum length of the pendant drop increases with increasing the initial diameter and the initial mass flow rate, whereas that decreases under the electric field.

3) The main influencing factor of the maximum length of the pendant drop without the electric field is the initial mass flow rate in most cases, but the initial diameter becomes the main influencing factor in some range of the initial diameter and the initial mass flow rate. By contrast, the main influencing factor under the electric field is only the initial mass flow rate.

4) The bridging of adjacent sheds by complete pendant drops is a relatively rare occurrence.

APPENDIX
A. EFFECTS OF INTERFACE THICKNESS CONTROL PARAMETER ON THE SIMULATION RESULTS
As the interface is diffused, the interface thickness control parameter β in the level-set equation (9) is important, so it is necessary to explore the effects of β on simulation results. Due to the importance of the length of a pendant drop and the
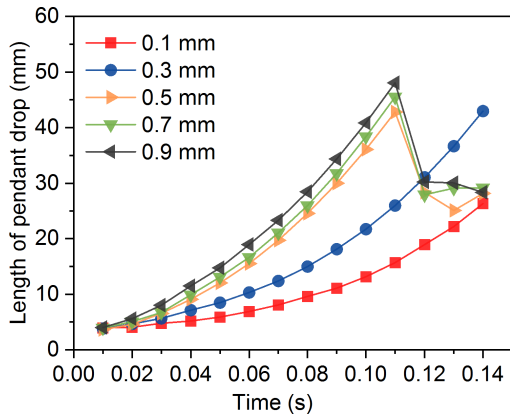
FIGURE 16. Lengths of the pendant drop at the different interface thickness control parameter varying with time.
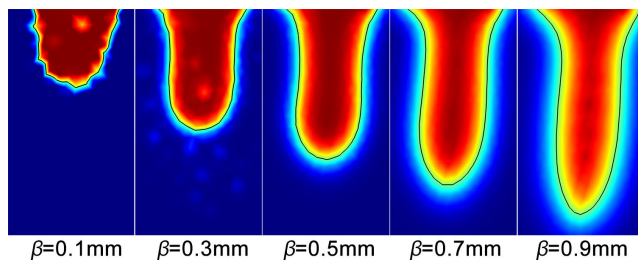

FIGURE 17. The interface of the pendant drop at the different interface thickness control parameter as *t* = 0.06 s.
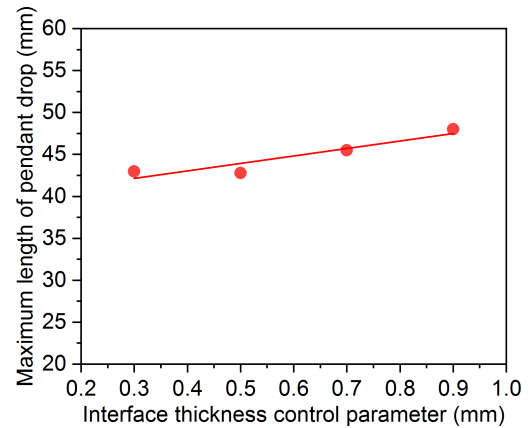

FIGURE 18. The maximum length of the pendant drop varying with different interface thickness control parameters.

relationship between L_{max} and β is

$$L_{\max} = 39.5 + 8.9\beta \qquad (30)$$

The ratio of the relative variation of L_{max} to β s used as the sensitivity of L_{max} to β, given as

$$S(L_{\max}, \beta) = \frac{\Delta L_{\max}/L_{\max}}{\Delta\beta/\beta} \qquad (31)$$

when $\Delta\beta \to 0$

$$S(L_{\max}, \beta) = \frac{dL_{\max}}{d\beta} \cdot \frac{\beta}{L_{\max}} \qquad (32)$$

From (30) and (32), the sensitivity of L_{max} to β is

$$S(L_{\max}, \beta) = \frac{8.9\beta}{L_{\max}} \qquad (33)$$

Calculated by (33), $S(L_{max}, \beta)$ at $\beta = 0.30$ mm, 0.50 mm, 0.70 mm and 0.90 mm are 0.06, 0.10, 0.14 and 0.17, respectively.

Finally, in view of the interface of the pendant drop (Fig. 17) and the sensitivity of L_{max} to β, 0.50 mm was taken as the interface thickness control parameter in the simulation.

B. TIME INTEGRATION

The backward difference method was used for the time integration. In Comsol, we adopted a variable order backward difference formula, which means that the higher-order formula is used first, whereas the lower-order one is automatically adopted for stability when necessary. The maximum and minimum order were set as two and one in the simulation, respectively. For the time step, an adaptive time-stepping scheme was used in the simulation. The solver tries to use the largest time step size, but it can reduce the time step size to meet the specified tolerance 10^{-3}, as solutions start to change rapidly in time. The time integral error was controlled by a nonlinear controller. When nonlinear failures occur, the nonlinear controller is activated and then more effectively controls the step size. Besides, the backward Euler method was used to consistently initialize the differential equations, which attempts to reconcile inconsistent initial values.

maximum length of a pendant drop L_{max}, we mainly analyzed the effects of β on them. According to Section II, β in this paper is half the size of the maximum unit of the mesh in the computational domain B, namely 0.50 mm. Therefore, We varied β from 0.10 mm to 0.90 mm at 0.20 mm interval. For simplifying the study, we took it at $d_i = 7.00$ mm and $u_i = 1.50$ g/s as an example.

Fig. 16 shows the length of the pendant drop varying with time at different β. As $\beta = 0.10$ mm and 0.30 mm, the lengths of the pendant drop increase with time, and the breakup of the pendant drop does not happen. Moreover, L_{max} is much smaller than that at the other β as $\beta = 0.10$ mm. As $\beta = 0.50$ mm, 0.70 mm, and 0.90 mm, the lengths of the pendant drop all increase first and then decrease with time, and they break up at 0.11s.

In order to select the suitable β, we analyzed the interface of the pendant drop, as shown in Fig. 17. Fig. 17 shows the interface of the pendant drop with different β at $t = 0.06$ s. As β is less than 0.50 mm, The distribution of the interface layers is non-uniform, and the interface has poor smoothness, especially as $\beta = 0.10$ mm, which indicates that the simulation results are not accurate as $\beta = 0.10$ mm.

To determine β used in the simulation, we explored the variation of L_{max} with different β and carried out sensitivity analysis. Considering that the simulation results are not accurate as $\beta = 0.10$ mm, we ignored L_{max} at $\beta = 0.10$ mm. L_{max} varying with different β is shown in Fig. 18. As β increases, L_{max} increases slightly, and the quantitative

We used a damped Newton method to solve nonlinear algebraic equations obtained by the time integration. The initial and minimum damping factors are 10^{-4} and 10^{-8}, respectively. When the estimated relative error is less than the specified tolerance or the maximum number of iterations reaches 20, the computation is terminated.

REFERENCES

[1] W. McDermid and T. Black, "Experience with preventing external flashovers in HVDC converter stations," in *Proc. Conf. Rec. IEEE Int. Symp. Elect. Insul.*, Jun. 2008, pp. 81–84.

[2] M. Ohba and S. Sugimoto, "Differences in climate change impacts between weather patterns: Possible effects on spatial heterogeneous changes in future extreme rainfall," *Climate Dyn.*, vol. 52, nos. 7–8, pp. 4177–4191, Apr. 2019.

[3] C. Zhang, L. Wang, and Z. Guan, "Investigation of DC discharge behavior of polluted porcelain post insulator in artificial rain," *IEEE Trans. Dielectr. Electr. Insul.*, vol. 23, no. 1, pp. 331–338, Feb. 2016.

[4] A. Bojovschi, W. S. T. Rowe, and K. L. Wong, "The influence of hanging water droplets on discharge activity, application to high voltage insulators," *Appl. Phys. Lett.*, vol. 98, no. 9, pp. 1–3, Feb. 2011.

[5] C. H. A. Ely, P. J. Lambeth, and J. S. T. Looms, "The booster shed: Prevention of flashover of polluted substation insulators in heavy wetting," *IEEE Trans. Power App. Syst.*, vol. PAS-97, no. 6, pp. 2187–2197, Nov. 1978.

[6] Y. Li, H. Jin, S. Nie, P. Zhang, and N. Gao, "Dynamic behavior of water droplets and flashover characteristics on a superhydrophobic silicone rubber surface," *Appl. Phys. Lett.*, vol. 110, no. 20, pp. 1–4, May 2017.

[7] S. Wei, H. Jin, H. Zhou, K. Yang, N. Gao, and W. Li, "Dynamic behavior of water droplets on wetted superhydrophobic surfaces under a high AC electric field," *AIP Adv.*, vol. 9, no. 6, pp. 1–6, Jun. 2019.

[8] J. Ndoumbe, A. Beroual, and A. M. Imano, "Simulation and analysis of coalescence of water droplets on composite insulating surface under DC electric field," *IEEE Trans. Dielectr. Electr. Insul.*, vol. 22, no. 5, pp. 2669–2675, Oct. 2015.

[9] Y. Liu, X. Kong, Y. Wu, and B. Du, "Dynamic behavior of droplets and flashover characteristics for CFD and experimental analysis on SiR composites," *IEEE Access*, vol. 7, pp. 8095–8101, 2019.

[10] Y. Liu, Y. Wu, and B. Du, "Dynamic formation mechanism of water droplet and induced surface discharges on silicone rubber composites," *High Voltage*, vol. 4, no. 1, pp. 59–64, Mar. 2019.

[11] A. Bateni, A. Ababneh, J. A. W. Elliott, A. W. Neumann, and A. Amirfazli, "Effect of gravity and electric field on shape and surface tension of drops," *Adv. Space Res.*, vol. 36, no. 1, pp. 64–69, Jan. 2005.

[12] B. Ambravaneswaran, H. J. Subramani, S. D. Phillips, and O. A. Basaran, "Dripping-jetting transitions in a dripping faucet," *Phys. Rev. Lett.*, vol. 93, no. 3, pp. 1–4, Jul. 2004.

[13] H. J. Subramani, H. K. Yeoh, R. Suryo, Q. Xu, B. Ambravaneswaran, and O. A. Basaran, "Simplicity and complexity in a dripping faucet," *Phys. Fluids*, vol. 18, no. 3, pp. 1–13, Mar. 2006.

[14] T. N. Nogueira, F. A. C. Pereira, J. Procopio, and J. C. Sartorelli, "Dripping faucet dynamics in a nonuniform electric field," *Chaos*, vol. 28, no. 11, pp. 1–6, Nov. 2018.

[15] P. K. Notz and O. A. Basaran, "Dynamics of drop formation in an electric field," *J. Colloid Interface Sci.*, vol. 213, no. 1, pp. 218–237, May 1999.

[16] M. P. Borthakur, G. Biswas, and D. Bandyopadhyay, "Dynamics of drop formation from submerged orifices under the influence of electric field," *Phys. Fluids*, vol. 30, no. 12, pp. 1–11, Dec. 2018.

[17] S. Rajendran, M. A. Jog, and R. M. Manglik, "Experimental investigation of jet breakup at low weber number," *Atomization Sprays*, vol. 27, no. 9, pp. 821–834, 2017.

[18] P. H. Son and K. Ohba, "Theoretical and experimental investigations on instability of an electrically charged liquid jet," *Int. J. Multiphase Flow*, vol. 24, no. 4, pp. 605–615, Jun. 1998.

[19] B. Nath, G. Biswas, and A. Dalal, "Influence of electric field on deformation of a drop in shear flow," *Phys. Fluids*, vol. 31, no. 4, pp. 1–13, Apr. 2019.

[20] Z. Wang, K. Dong, L. Tian, J. Wang, and J. Tu, "Numerical study on coalescence behavior of suspended drop pair in viscous liquid under uniform electric field," *AIP Adv.*, vol. 8, no. 8, pp. 1–13, Aug. 2018.

[21] R. Singh, S. S. Bahga, and A. Gupta, "Electric field induced droplet deformation and breakup in confined shear flows," *Phys. Rev. Fluids*, vol. 4, no. 3, pp. 1–24, Mar. 2019.

[22] X. Yang, A. J. James, J. Lowengrub, X. Zheng, and V. Cristini, "An adaptive coupled level-set/volume-of-fluid interface capturing method for unstructured triangular grids," *J. Comput. Phys.*, vol. 217, no. 2, pp. 364–394, Sep. 2006.

[23] A. Amani, N. Balcázar, J. Castro, and A. Oliva, "Numerical study of droplet deformation in shear flow using a conservative level-set method," *Chem. Eng. Sci.*, vol. 207, pp. 153–171, Nov. 2019.

[24] Q. Dong and A. Sau, "Breakup of a leaky dielectric drop in a uniform electric field," *Phys. Rev. E, Stat. Phys. Plasmas Fluids Relat. Interdiscip. Top.*, vol. 99, no. 4, pp. 1–29, Apr. 2019.

[25] J. Eggers, "Nonlinear dynamics and breakup of free-surface flows," *Rev. Mod. Phys.*, vol. 69, no. 3, pp. 865–929, Jul. 1997.

[26] S. H. Guo and H. Guo, "Application of Laplace formula in additional pressure deduction of curved surface," *Appl. Mech. Mater.*, vols. 687–691, pp. 102–104, Nov. 2014.

LIN YANG (Member, IEEE) was born in Hunan, China, in 1984. He received the B.S. degree from Guangxi University, in 2007, and the Ph.D. degree from the South China University of Technology, China, in 2012. He is currently working with the School of Electric Power, South China University of Technology, where he has been an Associate Professor, since 2017. His research interests include HV outdoor insulation and on-line monitoring and fault diagnosis of electrical equipment.
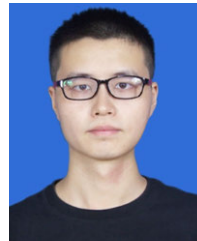
YIJIE SUN was born in Anhui, China, in 1995. He received the B.S. degree in electrical engineering from the China University of Mining and Technology, China, in 2018. He is currently pursuing the M.S. degree with the South China University of Technology, China. His research interest includes HV outdoor insulation.

YIFAN LIAO was born in Jiangxi, China, in 1987. He received the M.Sc. degree from the School of Electrical Engineering, Wuhan University, China, in 2012. He is currently pursuing the Ph.D. degree with the South China University of Technology. He is also working with the Electric Power Research Institute, China Southern Power Grid. His research interests include experimental research of HV technologies, HV engineering, and HV outdoor insulation. He is the author of 19 publications in the field of outdoor insulation.

ZHIQIANG KUANG was born in Jiangxi, China, in 1996. He received the B.S. degree in electrical engineering from the Nanjing University of Science and Technology, China, in 2018. He is currently pursuing the M.S. degree with the South China University of Technology, China. His research interest includes HV outdoor insulation.

YANPENG HAO (Member, IEEE) was born in Hebei, China, in 1974. She received the B.S. and Ph.D. degrees in electrical engineering from Xi'an Jiaotong University, China, in 1998 and 2003, respectively.

She has worked as a Postdoctoral Researcher with Tsinghua University, from 2003 to 2005. She is currently a Professor with the South China University of Technology, China. She is also the Leader of the High Voltage Group, SCUT. Her major research interests include condition perception and operation safety of transmission equipment, and atmospheric pressure dielectric barrier discharge. She is also a Commissioner of Professional Committee on High Voltage, Chinese Society for Electrical Engineering, a member of the Professional Committee on Engineering Dielectric, China Electrotechnical Society, and the Executive Chairman of 2nd IEEE International Conference on Electrical Materials and Power Equipment (ICEMPE 2019).

FUZENG ZHANG was born in Shandong, China, in 1979. He received the B.Sc. and M.Sc. degrees from the School of Automation, Northwestern Polytechnic University, China, in 2001 and 2004, respectively, and the Ph.D. degree from the Department of Electrical Engineering, Tsinghua University, Beijing, China, in 2008. He is currently working with the Ultra-High Voltage Laboratory, Technology Research Center, China Southern Power Grid. His research interests include HV engineering and HV outdoor insulation.

● ● ●

LICHENG LI was born in Jiangsu, China, in 1941. He received the B.S.E.E. degree from Tsinghua University, China, in 1967. From 1967 to 1980, he was with Gansu Electric Power Construction Corporation as the Chief Engineer. From 1980 to 1982, he was the Project Manager and the Principal Engineer of China Extra-High Voltage Technology Company. He joined China Southern Power Company (the Predecessor of China Southern Power Grid Company, CSG), in 1990, where he is currently the Secretary-General of the Consulting Group of CSG. He is currently a Professor with the South China University of Technology, China. His major research interests include HVAC/HVDC transmission networks, paralleling system operation and stability, and wide-area measurement and control.